Application of the finite volume method to the analysis of dynamic fracture problems

A. IVANKOVIC, I. DEMIRDZIC, J.G. WILLIAMS and P.S. LEEVERS
Mechanical Engineering Department, Imperial College of Science, Technology and Medicine, London SW7 2BX, U.K.

Abstract. A detailed description of a new numerical method for the solution of dynamic fracture problems is presented. The method employs finite volume discretization of the equilibrium equations.

The present work considers the analysis of rapid crack propagation (RCP) in two-dimensional geometries only. The simulation of steady-state RCP in a peeling-strip geometry, and an economical approach which allows the calculation of the crack driving force from a 'snapshot' computation of the displacement field are described. Also presented is the modelling of transient RCP in single edge notch tensile specimens, based on a fixed-mesh 'node release' technique and a 'holding back' force concept. It is shown that finite volume results are in very good agreement with both analytical and finite element predictions. The accuracy, simplicity and efficiency of this novel method are also demonstrated.

1. Introduction

Dynamic fracture is influenced by the effects of inertia and of stress wave propagation. Due to these, momentary values of the crack driving force (energy release rate) G^{dyn} and the stress intensity factor K^{dyn} during rapid crack propagation, cannot be derived from the crack length, loading and geometry as in static cases; a full dynamic analysis has to be performed. The presence of dynamic effects makes analytical solutions possible only for infinite geometries. Therefore, numerical simulation is often necessary for the analysis of RCP in real geometries.

A number of numerical schemes have been developed in order to solve solid mechanics problems involving dynamic fracture. These schemes usually utilise conventional mumerical methods such as Finite Difference, Finite Element (FE) and Boundary Element formulations. On the other hand, the Finite Volume (FV) method has been primarily used in solving fluid flow problems [1, 2]. However, it has recently been applied to the stress analysis of linear elastic [3], and elastic–plastic [4] solid materials, as an alternative to the widely used FE method. The only attempt so far to employ FV for the solution of dynamic fracture problems, has been conducted by the present authors; some preliminary results of FV simulation of a steady-state RCP along pressurised pipelines are presented in [5]. The FV method was demonstrated to be simple, straightforward, conservative and efficient, especially for nonlinear problems, due to its inherent iterative character. For these reasons, FV is employed in the present work for the analysis of RCP.
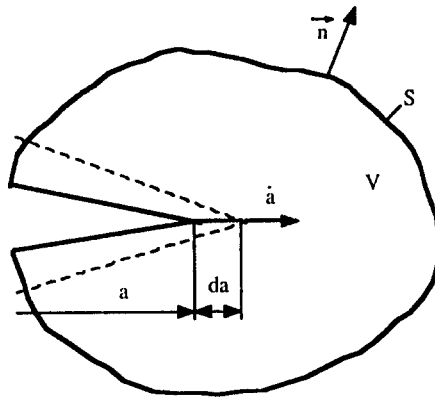
Fig. 1. A body with a moving crack.

2. Background

The basic problem in the analysis of a body of volume V, bounded by a surface S and containing a crack which propagates at a speed $\dot{a}$ (Fig. 1), is to solve the equation of motion at any instant of time t during the fracture event

$$\frac{\partial}{\partial t} \int_V \rho \frac{\partial u_i}{\partial t} \, dV = \int_S t_i \, dS + \int_V \rho f_i \, dV. \tag{1}$$

Here u_i is the displacement vector, $t_i = \sigma_{ij} n_j$ is the traction vector (surface force), σ_{ij} is the stress tensor, n_j is the unit vector of outward normal to the surfaces S, f_i is the body force and ρ is the mass density.

For an isotropic linear-elastic solid the relationship between the stresses σ_{ij} and strains ε_{ij} is

$$\sigma_{ij} = \lambda \varepsilon_{kk} \delta_{ij} + 2G \varepsilon_{ij}, \tag{2}$$

where $\lambda = \nu E/(1 + \nu)(1 - 2\nu)$ and $G = E/2(1 + \nu)$ are Lame constants, E is Young's modulus, ν is Poisson's ratio and δ_{ij} is the Kronecker delta.

For two-dimensional problems vector Eqn. (1) reduces to two scalar equations which, if body forces are neglected, represent the equilibrium of traction and inertia forces acting on the solid

$$\frac{\partial}{\partial t} \int_V \rho \frac{\partial u}{\partial t} \, dV = \int_S t_x \, ds, \tag{3a}$$

$$\frac{\partial}{\partial t} \int_V \rho \frac{\partial v}{\partial t} \, dV = \int_S t_y \, ds, \tag{3b}$$

where x and y are Cartesian coordinates, and u and v are displacements in x- and y-direction, respectively.

If a simple Cartesian control volume shown in Fig. 2 is considered, (3) take the form

$$\frac{\partial}{\partial t} \int_V \rho \frac{\partial u}{\partial t} \, dV = \left(\int_{S_n} t_{xn} \, dS - \int_{S_s} t_{xs} \, dS \right) + \left(\int_{S_e} t_{xe} \, dS - \int_{S_w} t_{xw} \, dS \right), \tag{4a}$$

$$\frac{\partial}{\partial t} \int_V \rho \frac{\partial v}{\partial t} \, \mathrm{d}V = \left(\int_{S_n} t_{yn} \, \mathrm{d}S - \int_{S_s} t_{ys} \, \mathrm{d}S \right) + \left(\int_{S_e} t_{ye} \, \mathrm{d}S - \int_{S_w} t_{yw} \, \mathrm{d}S \right). \qquad (4b)$$

By introducing (2) into (4) one obtains

$$\frac{\partial}{\partial t} \int_V \rho \frac{\partial u}{\partial t} \, \mathrm{d}V$$

$$\mathrm{Fin}_x$$

$$= \int_{S_n} G \left(\frac{\partial u}{\partial y} + \frac{\partial v}{\partial x} \right) \, \mathrm{d}S - \int_{S_s} G \left(\frac{\partial u}{\partial y} + \frac{\partial v}{\partial x} \right) \, \mathrm{d}S +$$

$$\qquad\qquad T_{xn} \qquad\qquad\qquad\qquad T_{xs}$$

$$+ \int_{S_e} \left((\lambda + 2G) \frac{\partial u}{\partial x} + \lambda \frac{\partial v}{\partial y} \right) \, \mathrm{d}S - \int_{S_w} \left((\lambda + 2G) \frac{\partial u}{\partial x} + \lambda \frac{\partial v}{\partial y} \right) \, \mathrm{d}S, \qquad (5a)$$

$$\qquad\qquad T_{xe} \qquad\qquad\qquad\qquad T_{xw}$$

$$\frac{\partial}{\partial t} \int_V \rho \frac{\partial v}{\partial t} \, \mathrm{d}V$$

$$\mathrm{Fin}_y$$

$$= \int_{S_e} G \left(\frac{\partial v}{\partial x} + \frac{\partial u}{\partial y} \right) \, \mathrm{d}S - \int_{S_w} G \left(\frac{\partial v}{\partial x} + \frac{\partial u}{\partial y} \right) +$$

$$\qquad\qquad T_{ye} \qquad\qquad\qquad\qquad T_{yw}$$

$$+ \int_{S_n} \left((\lambda + 2G) \frac{\partial v}{\partial y} + \lambda \frac{\partial u}{\partial x} \right) \, \mathrm{d}S - \int_{S_s} \left((\lambda + 2G) \frac{\partial v}{\partial y} + \lambda \frac{\partial u}{\partial x} \right) \, \mathrm{d}S. \qquad (5b)$$

$$\qquad\qquad T_{yn} \qquad\qquad\qquad\qquad T_{ys}$$

The problem reduces to the solution of (5) for displacements u and v. Having obtained the displacements throughout the body at any instant of time during RCP, the global energy balance

$$G^{\mathrm{dyn}} = \frac{1}{B\dot{a}} \left(\frac{\mathrm{d}U_E}{\mathrm{d}t} - \frac{\mathrm{d}U_S}{\mathrm{d}t} - \frac{\mathrm{d}U_K}{\mathrm{d}t} \right) = \frac{\mathrm{d}U_E}{\mathrm{d}A} - \frac{\mathrm{d}U_S}{\mathrm{d}A} - \frac{\mathrm{d}U_K}{\mathrm{d}A}, \qquad (6)$$

can be employed to determine either the crack length history, if RCP properties of the material under consideration are known, or the crack driving force G^{dyn} if the crack speed $\dot{a}$ is specified. Here, B is thickness, U_E is external work, U_S and U_K are strain and kinetic energies, respectively.

This paper considers only the generation mode analysis in which the crack length history, material mechanical properties, loading and boundary conditions are prescribed and corresponding G^{dyn} is generated.
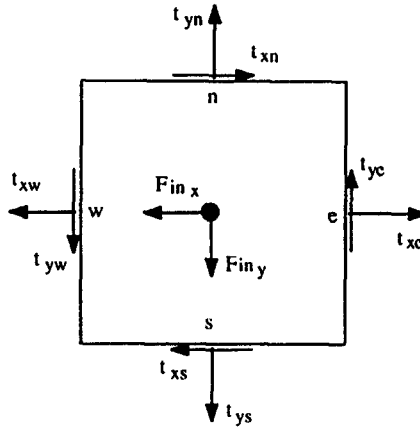
Fig. 2. Cartesian control volume and forces acting on it; n, s, e and w stand for north, south, east and west, respectively.
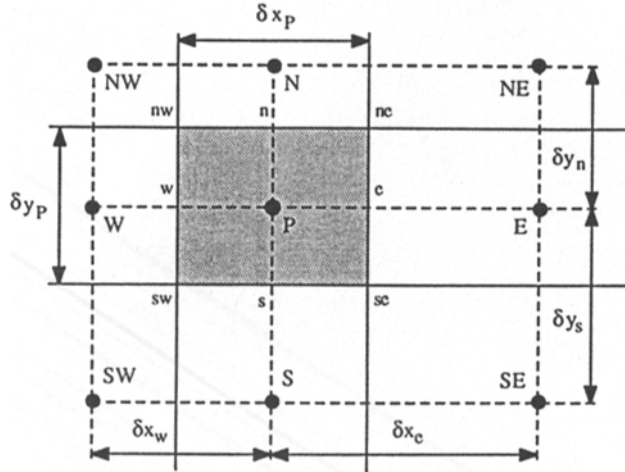

Fig. 3. Finite volume discretization; $\delta x_s = \delta x_n = \delta x_P$, $\delta y_w = \delta y_e = \delta y_P$, $S_s = \delta x_s B$, $S_n = \delta x_n B$, $S_w = \delta y_w B$, $S_e = \delta y_e B$.

3. The finite volume analysis

In order to solve the equations of motion (5), the FV discretization scheme is used. The time domain is divided into a number of discrete time steps δt, while the space domain is divided into a number of rectangular cells. Each cell is bounded by four faces with areas S_k ($k = n$, s, e, w), and it contains one computational nodal point at its centre (Fig. 3). The deformation of the cell is neglected in the analysis. Linear distribution of the displacements u and v between neighbouring points is assumed.

When the simulation of transient RCP is considered, the inertia force is approximated using the mean value theorem which gives

$$\text{Fin}_x = \rho V_P \frac{u_P^+ - 2u_P^0 + u_P^-}{\delta t^2}, \tag{7a}$$

$$\text{Fin}_y = \rho V_P \frac{v_P^+ - 2v_P^0 + v_P^-}{\delta t^2}, \tag{7b}$$

where superscripts '+', '0' and '−' refer to the 'future', 'present' and 'previous' time instants respectively and V_P is the volume of the cell. As the calculation of displacements '+' is completed, the solution is stepped forward by δt to the following time instant. In the first time step a non-existing value '−' is approximated by a corresponding value '0'. A fully implicit time differencing scheme is used, implying that all dependent variables correspond to '+' time instant, except in transient term (7). For convenience, the subscript '+' is omitted in the rest of this paper.

In modelling of steady state RCP, during which an observer travelling with the crack at a constant speed would observe no local change in the stress field, time is eliminated from the analysis and the inertia force is expressed as:

$$\text{Fin}_x = \rho(\dot{a})^2 \left(\frac{S_e}{\delta x_e}(u_E - u_P) - \frac{S_w}{\delta x_w}(u_P - u_W) \right), \tag{8a}$$

$$\text{Fin}_y = \rho(\dot{a})^2 \left(\frac{S_e}{\delta x_e}(v_E - v_P) - \frac{S_w}{\delta x_w}(v_P - v_W) \right). \tag{8b}$$

When Eqns. (5) are applied to an arbitrary cell containing the node P (Fig. 3), the forces acting on the cell faces are approximated using a central spatial differencing scheme as

x-direction

$$
\begin{aligned}
T_{xn} &= G_n \frac{S_n}{\delta y_n}(u_N - u_P) + G_n \frac{S_n}{\delta x_n}(v_{ne} - v_{nw}), \\
T_{xs} &= G_s \frac{S_s}{\delta y_s}(u_P - u_S) + G_s \frac{S_s}{\delta x_s}(v_{se} - v_{sw}), \\
T_{xe} &= (\lambda + 2G)_e \frac{S_e}{\delta x_e}(u_E - u_P) + \lambda_e \frac{S_e}{\delta y_e}(v_{ne} - v_{se}), \\
T_{xw} &= (\lambda + 2G)_w \frac{S_w}{\delta x_w}(u_P - u_W) + \lambda_w \frac{S_w}{\delta y_w}(v_{nw} - v_{sw}).
\end{aligned}
\tag{9a}
$$

y-direction

$$
\begin{aligned}
T_{yn} &= (\lambda + 2G)_n \frac{S_n}{\delta y_n}(v_N - v_P) + \lambda_n \frac{S_n}{\delta x_n}(u_{ne} - u_{nw}), \\
T_{ys} &= (\lambda + 2G)_s \frac{S_s}{\delta y_s}(v_P - v_S) + \lambda_s \frac{S_s}{\delta x_s}(u_{se} - u_{sw}), \\
T_{ye} &= G_e \frac{S_e}{\delta x_e}(v_E - v_P) + G_e \frac{S_e}{\delta y_e}(u_{ne} - u_{se}), \\
T_{yw} &= G_w \frac{S_w}{\delta x_w}(v_P - v_W) + G_w \frac{S_w}{\delta y_w}(u_{nw} - u_{sw}),
\end{aligned}
\tag{9b}
$$

Table 1. Coefficients and source terms in FV discretization

	A_N	A_S	A_E	A_W	a_p-transient
x	$G_n \dfrac{S_n}{\delta y_n}$	$G_s \dfrac{S_s}{\delta y_s}$	$(\lambda + 2G)_e \dfrac{S_e}{\delta x_e}$	$(\lambda + 2G)_w \dfrac{S_w}{\delta x_w}$	$\rho \dfrac{V_P}{\delta t^2}$
y	$(\lambda + 2G)_n \dfrac{S_n}{\delta y_n}$	$(\lambda + 2G)_s \dfrac{S_s}{\delta y_s}$	$G_e \dfrac{S_e}{\delta x_e}$	$G_w \dfrac{S_w}{\delta x_w}$	$\rho \dfrac{V_P}{\delta t^2}$

	b_{ns}	b_{ew}
x	$G_n \dfrac{S_n}{\delta x_n}(v_{ne} - v_{nw}) - G_s \dfrac{S_s}{\delta x_s}(v_{se} - v_{sw})$	$\lambda_e \dfrac{S_e}{\delta y_e}(v_{ne} - v_{se}) - \lambda_w \dfrac{S_w}{\delta y_w}(v_{nw} - v_{sw})$
y	$\lambda_n \dfrac{S_n}{\delta x_n}(u_{ne} - u_{nw}) - \lambda_s \dfrac{S_s}{\delta x_s}(u_{se} - u_{sw})$	$G_e \dfrac{S_e}{\delta y_e}(u_{ne} - u_{se}) - G_w \dfrac{S_w}{\delta y_w}(u_{nw} - u_{sw})$

	b_{in}-transient	b_{in}-steady state
x	$\rho \dfrac{V_P}{\delta t^2}(2u_P^0 - u_P^-)$	$-\rho(\dot a)^2 \left(\dfrac{S_e}{\delta x_e}(u_E - u_P) - \dfrac{S_w}{\delta x_w}(u_P - u_W) \right)$
y	$\rho \dfrac{V_P}{\delta t^{2.}}(2v_P^0 - v_P^-)$	$-\rho(\dot a)^2 \left(\dfrac{S_e}{\delta x_e}(v_E - v_P) - \dfrac{S_w}{\delta x_w}(v_P - v_W) \right)$

where, for example, the displacement u_{ne} at the cell corner is linearly interpolated between displacements of four surrounding points P, E, N, NE (Fig. 3)

$$u_{ne} = (u_P(1 - fx_P) + u_E fx_P)(1 - fy_P) + (u_N(1 - fx_P) + u_{NE} fx_P)fy_P,$$

$$fx_P = \frac{\delta x_P}{\delta x_P + \delta x_E}; \quad fy_P = \frac{\delta y_P}{\delta y_P + \delta y_N}.$$

As a result of FV discretization two algebraic equations are obtained for each cell

$$A_P u_P - \sum_K A_K u_K = b, \tag{10a}$$

$$A_P v_P - \sum_K A_K v_K = b, \tag{10b}$$

where $A_P = \Sigma_K A_K + a_P$, $b = b_{ns} + b_{ew} + b_{in}$, $K = N$, S, E, W, and the coefficients A_K and source term b are as listed in Table 1.

The most marked feature of the FV method is its conservative nature, i.e. the forces acting on the internal cell faces are always balanced.

The formulation of a particular problem is completed by specifying boundary conditions. These are implemented either by replacing the expressions for the traction forces in (9) by known boundary forces for given boundary cells, or by prescribing the displacements of the

boundary points. In the transient case initial conditions must be prescribed prior to dynamic solution (see Section 4.2).

Thus, a system of $2N$ linear algebraic equations with $2N$ unknown displacements $(u_1, \ldots, u_N, v_1, \ldots, v_N)$ is formed, where N is the number of cells. In order to solve this system, an iterative method is employed. The values of displacements in b, (10), are assumed known; in the first iteration guessed values are used, while values calculated from the previous iteration are used during the rest of the iterative process. Thus, the equations are temporarily decoupled for individual displacements, and two sets of N equations with a sparse five-diagonal diagonally dominant symmetric coefficient matrix are obtained. Equations are solved sequentially in turn by a line-by-line three diagonal matrix algorithm [1]. The process is repeated until a required convergence is achieved. In the transient case, the solution is then advanced to the next time step.

4. Applications

4.1. STEADY-STATE RCP IN A PEELING-STRIP GEOMETRY

After the method had been verified on a number of simple test cases (e.g. beams loaded in pure shear, tension and bending), it was applied to the analysis of steady-state RCP in the peeling-strip geometry. Williams [6] analysed a long strip of finite height H and thickness B, loaded by linearly varying pressure $p(x)$ over the distance λ and fracturing along its length at a constant speed $\dot{a}$ (Fig. 4). The expression for the dynamic crack driving force was derived from the global energy balance (6), using one-dimensional 'built-in' beam theory

$$\frac{G^{\text{dyn}}}{G^{\text{st}}} = 36 \frac{(\xi - \sin \xi)^2}{\xi^6}, \tag{11}$$

where $\xi \equiv \sqrt{12}(\lambda/H)(\dot{a}/C)$ and $C = \sqrt{(E/\rho)}$ is the longitudinal stress wave speed, while the static energy release rate G^{st} is given as

$$G^{\text{st}} = \frac{1}{6} \frac{B p_0^2 (\lambda^*)^4}{E H^3}.$$

Here a corrected length

$$\lambda^* = \lambda + \frac{2}{3} H,$$

accounts for deflection due to shear in the beam, and deflection due to rotation at its 'built-in' end.

The analytical prediction for the dynamic crack opening displacement v^{dyn} at $x = \lambda$ is derived in terms of the corresponding displacement v^{st} of a stationary crack

$$\frac{v^{\text{dyn}}}{v^{\text{st}}} = \frac{30}{\xi^4} \left(\frac{\xi^2}{3} + \cos \xi - \frac{\sin \xi}{\xi} \right). \tag{12}$$

The numerical simulation was performed by defining a control volume containing the crack front (Fig. 5). The pressure decay from p_0 to 0 is completed inside this volume, which cuts the bar at two vertical sections; one in front and the other behind the crack tip. Since steady-state conditions are assumed, fixing the control volume position relative to the crack tip which
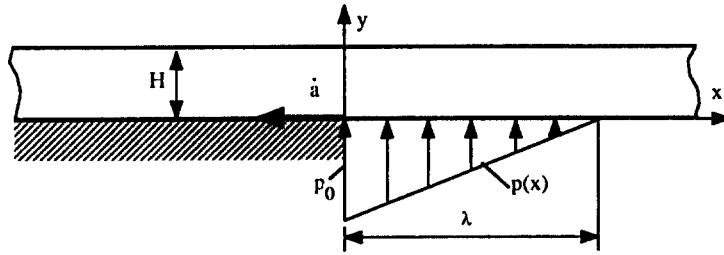
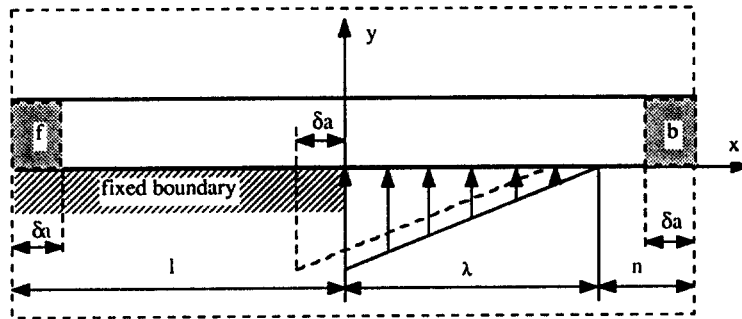*Fig. 4.* Peeling – strip geometry.

Fig. 5. Control volume for the analysis of peeling-strip geometry.

moves at a constant speed $\dot{a}$, the shape of the bar remains unchanged inside the volume. Thus, during an increment of crack growth δa, G^{dyn} is computed from the energy content of the bar as it enters and leaves the control volume, and the external work during the crack growth which is approximated as

$$\frac{1}{B}\frac{\mathrm{d}U_E}{\mathrm{d}a} = \frac{1}{B\,\mathrm{d}a}\left(\int_{x=0}^{x=\lambda} p(x)B\,\mathrm{d}x\right)\mathrm{d}v \approx \sum_{i=1}^{N_\lambda} p_i\,\frac{\delta v_1}{\delta a}\delta x_i,$$

where the summation is done over N_λ cells along the pressure decay length λ. So, (6) takes the form

$$G^{\text{dyn}} = \sum_{i=1}^{N_\lambda} p_i\,\frac{\delta v_i}{\delta a}\delta x_i + \frac{1}{B\delta a}(((U_s)_f - (U_s)_b) + ((U_k)_f - (U_k)_b)),\tag{13}$$

f and b stand for the front and back end regions of the bar respectively; e.g. $(U_k)_b$ is kinetic energy in the section $H \times \delta a \times B$ at the back end of the bar (Fig. 5). In this particular problem $(U_s)_f$, $(U_s)_b$ and $(U_k)_f$ are practically negligible.

The FV simulation was performed on a 1 m thick bar loaded by $p_0 = 1$ bar, with $H = 1 \times 10^{-3}$ m, $\lambda/H = 10$ and 8, $1 = 1 \times 10^{-2}$ m and $n = 1 \times 10^{-3}$ m. Material behaviour was characterized by $E = 1.5\,\text{GPa}$, $\nu = 0.33$ and $\rho = 1.5\;10^3\,\text{kg/m}^3$. As in the analytical solution, the bar is assumed to be under plane stress conditions. A mesh independent solution was achieved using a uniform mesh consisting of 525 rectangular cells for $\lambda/H = 10$ and 475 cells for $\lambda/H = 8$, with $\delta x = \delta y = 2 \times 10^{-4}$ m. δa was chosen to be equal to the length δx of the cell at the crack tip. However, varying δa showed little effect on G results once the solution had converged (Table 2).

Table 2. Influence of various δa on G results $(\lambda/H = 10)$

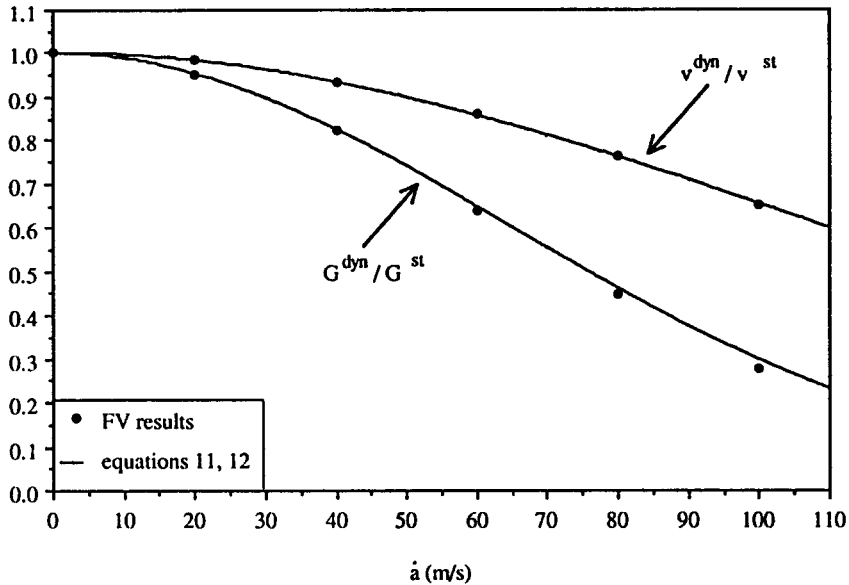|	G^{st} J/m^2	G^{dyn} J/m^2 $(\dot{a} = 100\,\text{m/s})$
$\delta a = 2 \times 10^{-4}$ m	14.32	9.09
$\delta a = 1 \times 10^{-4}$ m	14.72	9.20

Fig. 6. FV vs. analytical steady-state results $(\lambda/H = 10)$.

First, numerical simulation of a stationary crack $(\dot{a} = 0)$ was performed showing very good agreement with analytical results: within 1 percent for $\lambda/H = 10$ and 0.7 percent for $\lambda/H = 8$.

Computation for steady-state RCP was carried out for a range of crack speeds from 0 to 120 m/s. The comparisons between numerical and analytical G^{dyn} results are presented in Figs. 6 and 7, for $\lambda/H = 10$ and $\lambda/H = 8$, respectively. Values of the crack opening displacement at $x = \lambda$ are also shown.

Summarised G^{dyn} data from both $\lambda/H = 10$ and $\lambda/H = 8$ steady-state RCP simulations are presented in Fig. 8 in the form of a single master G^{dyn} vs. ξ curve. Figures 6 to 8 demonstrate remarkable agreement between FV and analytical results, verifying both the accuracy of the FV method and the validity of the approach for calculation of $G^{dyn\,(st)}$ (13).

4.2. TRANSIENT RCP IN SINGLE EDGE NOTCH TENSILE (SENT) GEOMETRIES

The accuracy of the FV method for transient RCP has been examined by comparing its results with those from idealised analytical and dynamic FE solutions [7]. FV modelling was performed on single-material SENT and duplex SENT geometries (Figs. 9 and 10), and all the details regarding the geometries, materials, crack speed data, loading and the boundary conditions are taken from [7].
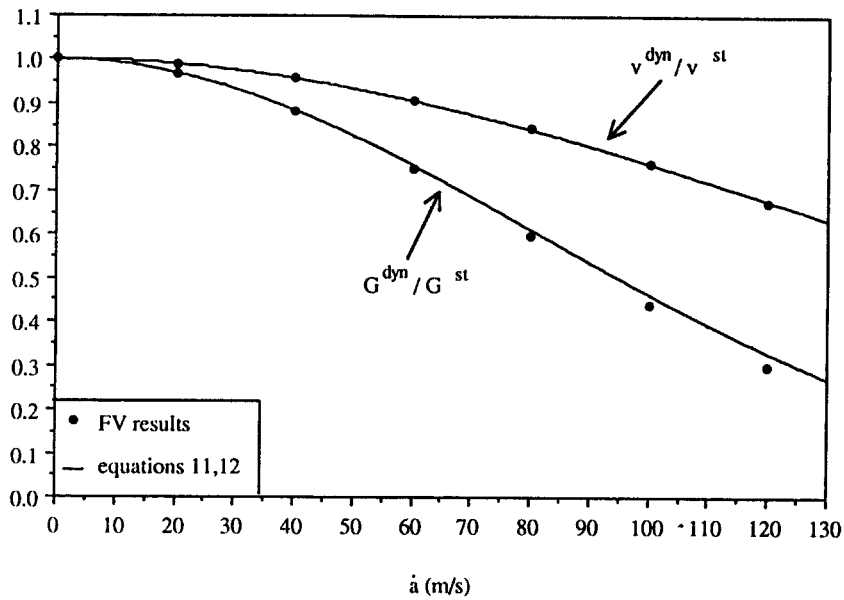
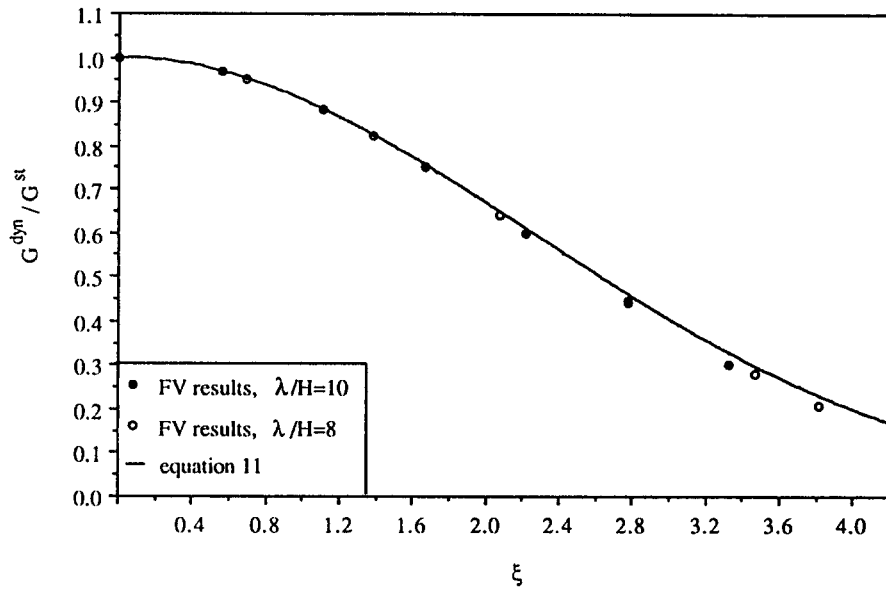*Fig. 7.* FV vs. analytical steady-state results $(\lambda/H = 8)$.

Fig. 8. FV vs. analytical steady-state G^{dyn} results.

Experience gained from the FE work on RCP has been useful in developing the FV code. The simulation of a propagating crack is based on a fixed mesh 'node release' technique, which is simpler than alternative moving mesh procedures [8, 9]. Only a generation mode analysis is considered in this work, i.e. the crack length history is prescribed and the corresponding crack driving force is generated. Due to symmetry, only half of the sample is analysed and the crack path is represented as a boundary. The running crack is modelled by sequential release of the boundary cell faces along the crack path, progressively changing boundary conditons. It was found that a step change of boundary conditions with instantaneous increase of the
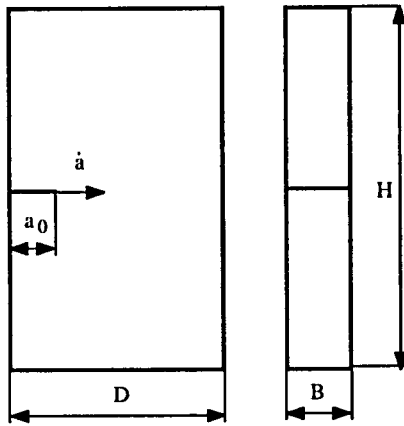
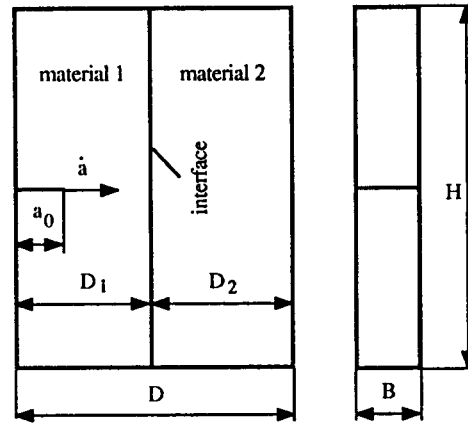*Fig. 9.* Single material SENT geometry.

Fig. 10. Duplex SENT geometry.

crack length by one element spacing caused spurious oscillations in the FE solution [8, 9]. Also, no net energy was dissipated in the system as the crack propagated. In the fixed mesh FE simulations, this problem was overcome by applying a 'holding back force' to the newly released node at the instant of release [8, 9 10]. This force was gradually decayed to zero from its maximum value, equal to the negative nodal force prior to release. A number of decay schemes have been proposed, and a linear decay of holding back force found to be satisfactory [11, 12], suppressing artificial oscillations and providing an energy sink near the moving crack tip. A similar concept is used in the present work. The holding back force (T_{ys}), applied on the last released boundary cell face, decreases gradually from its prior value $(T_{ys})_0$ according to the position of the crack tip

$$T_{ys} = -(T_{ys})_0(1 - f),$$ (14)

where $0 < f < 1$ is the proportion of cell face length traversed by the crack. When this reaches 1, the next boundary cell face is set free and the procedure is repeated.

Before the crack initiates, an initial static solution of the stresss-strain distribution in the sample is computed, corresponding to the static boundary conditions. Having obtained the initial conditions, the crack is propagated by releasing the boundary cell faces at times specified according to the crack speed. Every time a cell face is released, the energy absorbed by the crack is calculated by both global energy balance

$$G^{dyn} \approx \frac{(((U_E)_{tn} - (U_E)_{tp}) - ((U_S)_{tn} - (U_S)_{tp}) - ((U_K)_{tn} - (U_K)_{tp}))}{B\delta x_s},$$ (15)

and summation of the local work done by the holding back force

$$G^{dyn} \approx \sum_{tp}^{tn} \frac{(T_{ys})_t(v_t - v_{t-\delta t})}{B\delta x_s},$$ (16)

tn and tp stand for the times when the next and present crack tip cell faces, respectively, are released, t is the current time, $(T_{ys})_t$ is the current holding back force acting on the presently released cell face, and v_t and $v_{t-\delta t}$ are the crack tip opening displacements of the released boundary face node at two consecutive times. Both methods should agree if the solution is stable [8, 9, 12]. Disparity indicates that energy is not being conserved in the system.
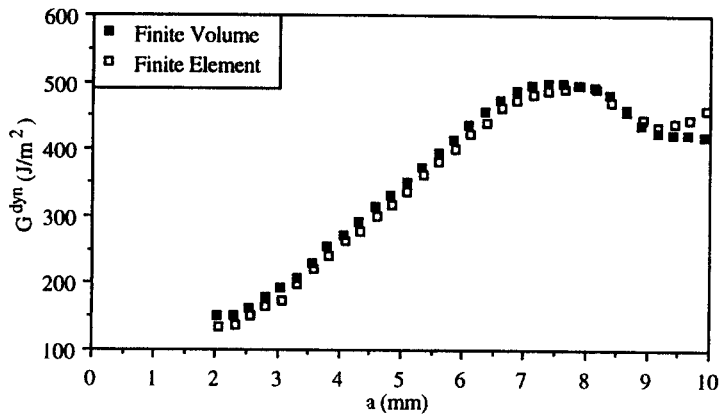
Fig. 11. Crack driving force vs. crack length; FV vs. FE results; $E = 6\,\text{GPa}$, $\nu = 0.33$, $\rho = 1180\,\text{kg/m}^3$, $D = 10\,\text{mm}$, $H = 40\,\text{mm}$, $P = 1.65\,\text{kN}$, $a_0 = 1.8\,\text{mm}$, $\dot{a} = 305\,\text{m/s}$; FV: 3200 nodes, FE: 3198 nodes.

A uniform mesh is used throughout, as recommended for the simulation of transient RCP [11, 12]. The sample is assumed to be under plane strain conditions. During static loading, a uniform y displacement, corresponding to the applied load is applied to the upper boundary, along which all boundary cell faces were constrained in the x-direction. The cell faces along the crack path were only constrained in the y-direction, while those along the initial notch a_0 (Figs. 9 and 10) and the two side boundaries were stress free.

The dynamic mode calculation begins by a release of the crack tip cell face. During the dynamic computation the specimens are regarded as being under fixed grip conditions, i.e. the upper boundary is fixed in both x- and y-directions. In the case of the duplex SENT sample, the mechanical properties of material were attributed to all cells on one side of the interface, while all cells on the other side had the mechanical properties of material 2 (Fig. 10). The forces acting on the cell faces which lie on the interface are calculated using a harmonic mean value of the mechanical properties of the two materials (E and G). Constant crack speed was specified throughout the single material SENT sample. In the duplex sample, the crack propagated at a constant speed in material 1, arrested at the interface for a short period (t_{arrest}), and continued with a lower constant speed through the second material.

Figures 11, 12 and 13 show the comparison between FV and FE G^{dyn} results. In the FE solution, uniform meshes consisting of constant strain triangular elements were used. Also shown in Fig. 12 are the static and dynamic infinite plate predictions

$$G^{\text{st}} = \frac{(K^{\text{st}})^2}{E}\,(1 - \nu^2) = \frac{P^2 \pi a}{B^2 D^2 E}\,(1 - \nu^2), \tag{17}$$

where K^{st} is a static stress intensity factor and P is the load prior to fracture, and

$$G^{\text{dyn}} = G^{\text{st}} g(\dot{a}), \tag{18}$$

$g(\dot{a})$ being the crack speed correction factor, which is equal to unity at zero crack speed and reduces to zero at Rayleigh surface wave speed. For the case presented in Fig. 12 $g(\dot{a}) = 0.88$ [13].

Generally, very good agreement between the FV and FE results is demonstrated. However, some disagreement developed as the crack approached the end of the sample, where only a few cells in FV or elements in FE simulation remained along the crack path. Therefore,
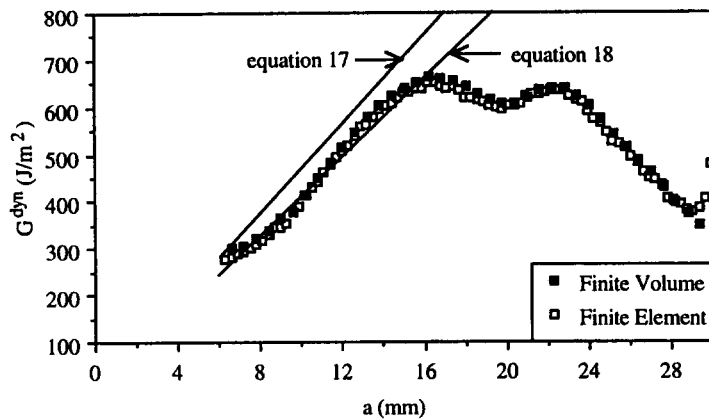
Fig. 12. Crack driving force vs. crack length; FV vs. FE vs. analytical results; $E = 6\,\text{GPa}$, $\nu = 0.33$, $\rho = 1180\,\text{kg/m}^3$, $D = 30\,\text{mm}$, $H = 80\,\text{mm}$, $P = 3.7\,\text{kN}$, $a_0 = 6\,\text{mm}$, $\dot{a} = 253.6\,\text{m/s}$; FV: 2500 nodes, FE: 14342 nodes.
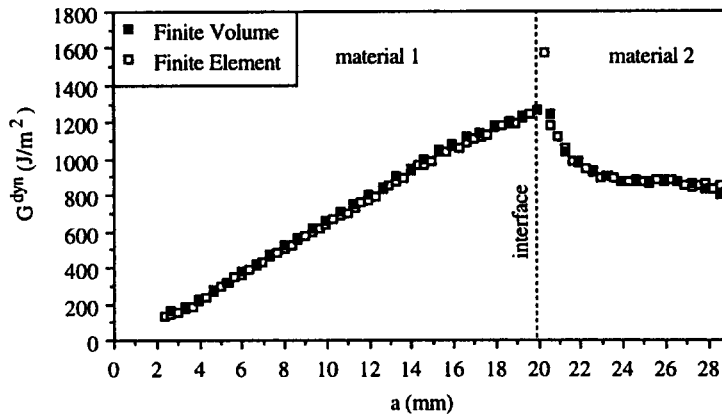

Fig. 13. Crack driving force vs. crack length; FV vs. FE results; $E_1 = 6\,\text{GPa}$, $\nu_1 = 0.33$, $\rho_1 = 1180\,\text{kg/m}^3$, $E_2 = 3\,\text{GPa}$, $\nu_2 = 0.39$, $\rho_2 = 1190\,\text{kg/m}^3$, $D_1 = 19.8\,\text{mm}$, $D_2 = 9.3\,\text{mm}$, $H = 100\,\text{mm}$, $P = 2.06\,\text{kN}$, $a_0 = 2\,\text{mm}$, $\dot{a}_1 = 344.3\,\text{m/s}$; $\dot{a}_2 = 265\,\text{m/s}$, $t_{\text{arrest}} = 1.2\,\mu\text{s}$; FV: 2640 nodes, FE: 14952 nodes.

neither of the two methods is expected to give accurate results. Unlike the static solution, the dynamic infinite plate prediction is in close agreement with numerical simulations of the finite size geometry. Until the stress waves return to the tip, the crack is 'unaware' of the specimen size; thereafter, some divergence starts to develop, although no abrupt step change due to the wave arrival itself occurs.

The influence of the mesh size on the FV results is shown in Fig. 14. The test shown in Fig. 11 is simulated using four different mesh sizes. It is demonstrated that the FV method is reasonably accurate (within 5 percent) even when a very coarse mesh (200 nodes) is used. When the same test was analysed by FE and the mesh size was reduced from original 3198 nodes to 756 nodes, the difference between corresponding results was found to be within 7 percent.

It is important to notice that since the implicit time differencing scheme is used (Section 3), the only restriction on the time step δt is imposed by the accuracy requirement. The insensitivity of the computed results to the range of $\delta t / tc$ ratios is shown in Fig. 15, where tc is the time for the longitudinal stress wave to travel between two nearest nodes in the mesh.
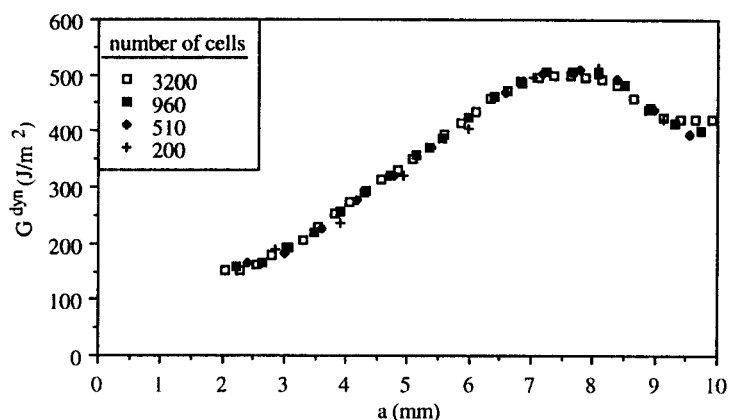
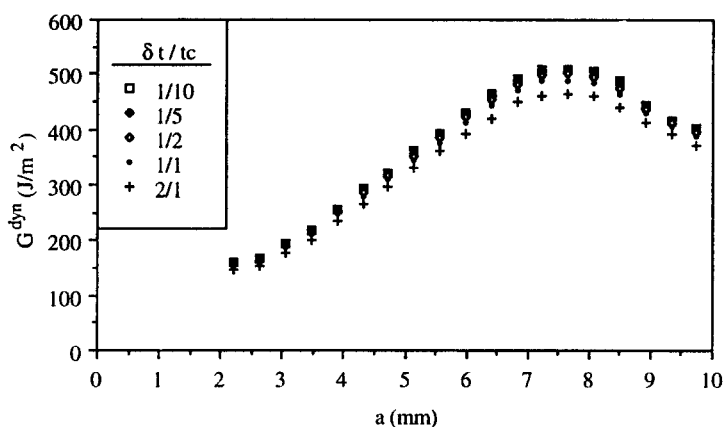*Fig. 14.* Influence of the mesh size on G^{dyn} vs. a results.

Fig. 15. Influence of the time step (δt) on G^{dyn} vs. a results.

Although the results presented in Figs. 11 to 14 were generated using $\delta t/tc = \frac{1}{5}$, the optimal results regarding the computing time can be achieved with $\delta t/tc = \frac{1}{2}$.

It is also worth mentioning that the FE code [7] required twice as much computer memory as the FV code for the same number of computational nodes.

5. Conclusions

A novel numerical approach has been introduced to the solution of dynamic fracture problems. The finite volume discretization of the equilibrium equations leads to a system of decoupled linear algebraic equations with sparse, symmetric and diagonally dominant coefficient matrices. Consequently, a low computational memory requirement is achieved. The equations were efficiently solved by line-by-line iterative solver.

The attractive simplicity is thought to be one of the main features of the presented technique; equally important is its conservative nature, which resulted in good accuracy even when coarse meshes were employed.

This paper has considered only the application of the method to two-dimensional linear elastic RCP problems. However, it was recently shown that FV can easily be applied to any

geometry using arbitrary cell topology [14]. Work is also being conducted in order to efficiently and accurately simulate RCP in three dimensional specimens made of nonlinear materials.

References

1. S.V. Patankar, *Numerical Heat Transfer and Fluid Flow*, McGraw Hill (1980).
2. I. Demirdzic, and M. Peric, *International Journal of Numerical Methods in Fluids* 10 (1990) 771.
3. I. Demirdzic, D. Martinovic and A. Ivankovic, *Zavarivanje* 31 (1988) 209, in Croatian.
4. I. Demirdzic and D. Martinovic, *Computational Methods in Applied Mechanics and Engineering*, 109 (1993) 331.
5. P.S. Leevers, G. Venizelos and A. Ivankovic, *Plastic Pipes VIII*, D1/7 (1992).
6. J.G. Williams, in *The Energetics of Fracture, The Griffith Centenary Meeting*, The Institute of Materials, London (1993) 96.
7. A. Ivankovic, Ph.D. thesis, University of London, Imperial College (1991).
8. P.N.R. Keegstra, J.L. Head and C.E. Turner, *Numerical Methods in Fracture Mechanics* (1978) 634.
9. B. Crouch, Ph.D. thesis, University of London, Imperial College (1986).
10. G. Yagawa, Y. Sakai and Y. Ando, *Fast Fracture and Crack Arrest, ASTM STP 627* (1977) 109.
11. J.F. Malluck and W.W. King, *Crack Arrest Methodology and Applications, ASTM STP 711* (1980) 38.
12. L. Hodulak, A.S. Kobayashi and A.F. Emery, *Fracture Mechanics: 12th Conference, ASTM STP 627* (1980) 177.
13. B.K. Broberg (ed.), *Recent Progress in Applied Mechanics*, Wiley (1967) 125.
14. I. Demirdzic and S. Muzaferija, *Numerical Methods in Engineering*, submitted for publication.